

AD-A283 688



①

ARMY RESEARCH LABORATORY

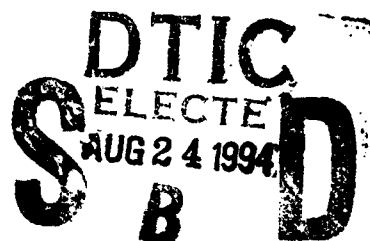


Numerical Computations of  
Supersonic Base Flow With  
Special Emphasis on  
Turbulence Modeling

Jubaraj Sahu

ARL-TR-438

June 1994



DTIC QUALITY INSPECTED 5

APPROVED FOR PUBLIC RELEASE; DISTRIBUTION IS UNLIMITED.

398

94-26903



94 8 23 1 13

## **NOTICES**

**Destroy this report when it is no longer needed. DO NOT return it to the originator.**

**Additional copies of this report may be obtained from the National Technical Information Service, U.S. Department of Commerce, 5285 Port Royal Road, Springfield, VA 22161.**

**The findings of this report are not to be construed as an official Department of the Army position, unless so designated by other authorized documents.**

**The use of trade names or manufacturers' names in this report does not constitute indorsement of any commercial product.**

**REPORT DOCUMENTATION PAGE**Form Approved  
OMB No. 0704-0188

Public reporting burden for this collection of information is estimated to average 1 hour per response, including the time for reviewing instructions, searching existing data sources, gathering and maintaining the data needed, and completing and reviewing the collection of information. Send comments regarding this burden estimate or any other aspect of this collection of information, including suggestions for reducing this burden, to Washington Headquarters Services, Directorate for Information Operations and Reports, 1215 Jefferson Davis Highway, Suite 1204, Arlington, VA 22202-4302, and to the Office of Management and Budget, Paperwork Reduction Project (0704-0188), Washington, DC 20503.

1. AGENCY USE ONLY (Leave blank)

2. REPORT DATE

June 1994

3. REPORT TYPE AND DATES COVERED

Final, Dec 91-Dec 92

4. TITLE AND SUBTITLE

Numerical Computations of Supersonic Base Flow With Special Emphasis on  
Turbulence Modeling

5. FUNDING NUMBERS

PR: 1L161102AH43  
61102A-00-001 AJ

6. AUTHOR(S)

Jubaraj Sahu

7. PERFORMING ORGANIZATION NAME(S) AND ADDRESS(ES)

U.S. Army Research Laboratory  
ATTN: AMSRL-WT-PB  
Aberdeen Proving Ground, MD 21005-5066

8. PERFORMING ORGANIZATION  
REPORT NUMBER

9. SPONSORING / MONITORING AGENCY NAME(S) AND ADDRESS(ES)

U.S. Army Research Laboratory  
ATTN: AMSRL-OP-AP-L  
Aberdeen Proving Ground, MD 21005-5066

10. SPONSORING / MONITORING  
AGENCY REPORT NUMBER

ARL-TR-438

11. SUPPLEMENTARY NOTES

This report supersedes BRL-IMR-971, June 1992.

12a. DISTRIBUTION / AVAILABILITY STATEMENT

Approved for public release; distribution is unlimited.

12b. DISTRIBUTION CODE

13. ABSTRACT (Maximum 200 words)

A zonal, implicit, time-marching Navier-Stokes computational technique has been used to compute the turbulent supersonic base flow over cylindrical afterbodies. A critical element of calculating such flows is the turbulence model. Various eddy viscosity turbulence models have been used in the base region flow computations. These models include two algebraic turbulence models and a two-equation k- $\epsilon$  model. The k- $\epsilon$  equations are developed in a general coordinate system and solved using an implicit algorithm. Calculations with the k- $\epsilon$  model are extended up to the wall. Flow field computations have been performed for a cylindrical afterbody at  $M = 2.46$  and at angle of attack  $\alpha = 0$ . The results are compared to the experimental data for the same conditions and the same configuration. Details of the mean flow field as well as the turbulence quantities have been presented. In addition, the computed base pressure distribution has been compared with the experiment. In general, the k- $\epsilon$  turbulence model performs better in the near wake than the algebraic models and predicts the base pressure much better.

14. SUBJECT TERMS

base flow, base pressure, turbulence models, wake, supersonic flow

15. NUMBER OF PAGES

34

16. PRICE CODE

17. SECURITY CLASSIFICATION  
OF REPORT

UNCLASSIFIED

18. SECURITY CLASSIFICATION  
OF THIS PAGE

UNCLASSIFIED

19. SECURITY CLASSIFICATION  
OF ABSTRACT

UNCLASSIFIED

20. LIMITATION OF ABSTRACT

UL

**INTENTIONALLY LEFT BLANK.**

## TABLE OF CONTENTS

	<u>Page</u>
LIST OF FIGURES .....	v
1. INTRODUCTION .....	1
2. GOVERNING EQUATIONS AND SOLUTION TECHNIQUE .....	2
2.1 Governing Equations .....	3
2.2 Numerical Technique .....	5
2.3 Composite Grid Scheme .....	6
2.4 Turbulence Modeling .....	7
2.4.1 Baldwin-Lomax Model .....	7
2.4.2 Chow Model .....	8
2.4.3 Two-Equation k- $\epsilon$ Model .....	9
3. MODELING GEOMETRY AND EXPERIMENT .....	12
4. RESULTS .....	12
5. CONCLUDING REMARKS .....	24
6. REFERENCES .....	25
LIST OF SYMBOLS .....	27
DISTRIBUTION LIST .....	29

**INTENTIONALLY LEFT BLANK.**

# LIST OF FIGURES

Figure	Page
1. Schematic Diagram of Supersonic Base Flow .....	2
2. Afterbody Measurement Locations .....	13
3. Base Region Computational Grid .....	14
4. Computed Pressure Contours in the Base Region, $M_\infty = 2.46$ , $\alpha = 0$ , and k- $\epsilon$ Model .....	15
5a. Computed Mach Contours, $M_\infty = 2.46$ , $\alpha = 0$ , and k- $\epsilon$ Model .....	15
5b. Experimental Schlieren Photograph .....	16
6. Velocity Vectors in the Base Region, $M_\infty = 2.46$ , $\alpha = 0$ , and k- $\epsilon$ Model .....	16
7. Streamwise Velocity (u) Profiles, $M_\infty = 2.46$ , $\alpha = 0$ .....	17
8. Normal Velocity (w) Profiles, $M_\infty = 2.46$ , $\alpha = 0$ .....	18
9. Turbulent Kinetic Energy Profiles, $M_\infty = 2.46$ , $\alpha = 0$ .....	20
10. Turbulent Dissipation Rate Profiles, $M_\infty = 2.46$ , $\alpha = 0$ .....	21
11. Turbulent Shear Stress Profiles, $M_\infty = 2.46$ , $\alpha = 0$ .....	22
12. Base Pressure Distribution, $M_\infty = 2.46$ , $\alpha = 0$ .....	23

Accession For	
NTIS GRA&I	<input checked="" type="checkbox"/>
DTIC TAB	<input type="checkbox"/>
Unannounced	<input type="checkbox"/>
Justification	
By	
Distribution/	
Availability Codes	
Dist	Avail and/or Special
A-1	

**INTENTIONALLY LEFT BLANK.**



## 1. INTRODUCTION

One of the important parameters in shell design is the total aerodynamic drag. The total drag consists of three components: the pressure drag or the wave drag (excluding the base), the viscous drag, and the base drag. The base drag component is a large part of the total drag and can be as high as 50% or more of the total drag. Of these three components of drag, the most difficult one to predict is the base drag because it depends on the pressure acting on the base. Therefore, it is necessary to predict the base pressure as accurately as possible.

The ability to compute the base region flow field for projectile configurations using Navier-Stokes computational techniques has been developed over the past few years (Sahu, Nietubicz, and Steger 1985; Sahu 1986, 1987). Recently, improved numerical predictions (Sahu and Steger 1988; Sahu 1990; Sahu and Nietubicz 1990) have been obtained using the Cray-2 supercomputer and a more advanced zonal upwind flux-split algorithm. This zonal scheme preserves the base corner and allows better modeling of the base region flow. These studies have included base flows for different base geometries. This capability is very important for determining aerodynamic coefficient data, including the total aerodynamic drag. As indicated earlier, a number of base flow calculations have been made, and base drag and total drag have been predicted with reasonable accuracy. However, because available data are lacking, the predictive capabilities have not been assessed with detailed base pressure distributions, mean flow velocity components, and turbulence quantities. This is especially true of base flow for axisymmetrical bodies at transonic and supersonic speeds. Recently, experimental measurements (Herrin and Dutton 1991) have been made in the base region for supersonic flow over a cylindrical afterbody. The data include base pressure distribution (along the base), mean flow, and turbulence quantities.

Figure 1 is a schematic diagram showing the important features of supersonic base flow. The approaching supersonic turbulent boundary layer separates at the base corner, and the free shear layer region is formed in the wake. The flow expands at the base corner and is followed by the recompression shock downstream from the base that realigns the flow. The flow then redevelops in the trailing wake. A low pressure region is formed immediately downstream from the base, which is characterized by a low speed recirculating flow region. Interaction between this recirculating region and the inviscid external flow occurs through the free shear mixing region. This is the region where turbulence plays an important role.

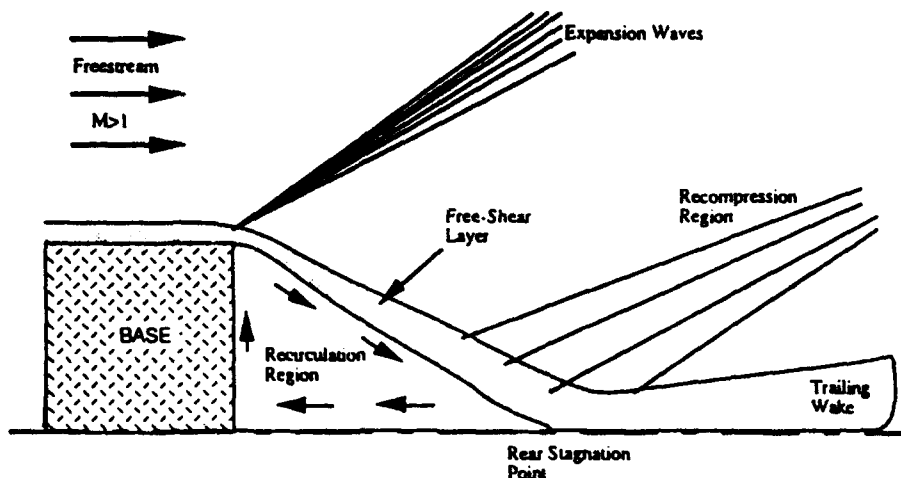


Figure 1. Schematic Diagram of Supersonic Base Flow.

The basic configuration used in this study is a cylindrical afterbody. As mentioned earlier, a simple composite grid scheme has been used for accurate modeling of the base corner. Numerical flow field computations have been performed at  $M_\infty = 2.46$  and at  $0^\circ$  angle of attack. Three turbulence models (two algebraic models and a two-equation model) are used in the base flow region. All the computations have been performed on the Cray-XMP supercomputer. Details of the flow field such as Mach number contours and base pressure distributions are presented. Computed base pressure distributions are compared with available experimental data for the same conditions and the same configuration. The algebraic turbulence models predict a large change in the base pressure distribution over the base. The two-equation  $k-\epsilon$  model predicts a rather small change in base pressure along the base and compares very well with the experimentally measured base pressure distribution.

## 2. GOVERNING EQUATIONS AND SOLUTION TECHNIQUE

The complete set of time-dependent, Reynolds-averaged, thin layer Navier-Stokes equations is solved numerically to obtain a solution to this problem. The numerical technique used is an implicit, finite difference scheme. Although time-dependent calculations are made, the transient flow is not of primary interest at the present time. The steady flow, which is the desired result, is obtained in a time asymptotic fashion.

**2.1 Governing Equations.** The complete set of three-dimensional (3-D), time-dependent, generalized geometry, Reynolds-averaged, thin layer, Navier-Stokes equations for general spatial coordinates  $\xi$ ,  $\eta$ , and  $\zeta$  can be written as (Pulliam and Steger 1982)

$$\partial_\tau \hat{Q} + \partial_\xi \hat{F} + \partial_\eta \hat{G} + \partial_\zeta \hat{H} = Re^{-1} \partial_\zeta \hat{S} \quad (1)$$

in which

$\xi = \xi(x, y, z, t)$  - longitudinal coordinate;  $\eta = \eta(x, y, z, t)$  - circumferential coordinate

$\zeta = \zeta(x, y, z, t)$  - nearly normal coordinate;  $\tau = t$  - time

and

$$\hat{Q} = \frac{1}{J} \begin{bmatrix} \rho \\ \rho u \\ \rho v \\ \rho w \\ e \end{bmatrix} \quad \hat{F} = \frac{1}{J} \begin{bmatrix} \rho U \\ \rho u U + \xi_x p \\ \rho v U + \xi_y p \\ \rho w U + \xi_z p \\ (e + p)U - \xi_x p \end{bmatrix}$$

$$\hat{G} = \frac{1}{J} \begin{bmatrix} \rho V \\ \rho u V + \eta_x p \\ \rho v V + \eta_y p \\ \rho w V + \eta_z p \\ (e + p)V - \eta_x p \end{bmatrix} \quad \hat{H} = \frac{1}{J} \begin{bmatrix} \rho W \\ \rho u W + \zeta_x p \\ \rho v W + \zeta_y p \\ \rho w W + \zeta_z p \\ (e + p)W - \zeta_x p \end{bmatrix} \quad (2)$$

and in which

$$\hat{S} = \frac{1}{J} \begin{bmatrix} 0 \\ \mu(\zeta_x^2 + \zeta_y^2 + \zeta_z^2)u_\zeta + \frac{\mu}{3}(\zeta_x u_\zeta + \zeta_y v_\zeta + \zeta_z w_\zeta)\zeta_x \\ \mu(\zeta_x^2 + \zeta_y^2 + \zeta_z^2)v_\zeta + \frac{\mu}{3}(\zeta_x u_\zeta + \zeta_y v_\zeta + \zeta_z w_\zeta)\zeta_y \\ \mu(\zeta_x^2 + \zeta_y^2 + \zeta_z^2)w_\zeta + \frac{\mu}{3}(\zeta_x u_\zeta + \zeta_y v_\zeta + \zeta_z w_\zeta)\zeta_z \\ \left\{ (\zeta_x^2 + \zeta_y^2 + \zeta_z^2) \left[ \frac{\mu}{2}(u^2 + v^2 + w^2)_\zeta + \frac{\kappa a_\zeta^2}{Pr(\gamma-1)} \right] + \frac{\mu}{3}(\zeta_x u + \zeta_y v + \zeta_z w)(\zeta_x u_\zeta + \zeta_y v_\zeta + \zeta_z w_\zeta) \right\} \end{bmatrix} \quad (3)$$

In Equation 1, the thin layer approximation is used and the viscous terms involving velocity gradients in both the longitudinal and circumferential directions are neglected. The viscous terms are retained in the normal direction,  $\zeta$ , and are collected into the vector  $\hat{S}$ . These viscous terms are used everywhere. However, in the wake or the base region, similar viscous terms are also added in the stream-wise direction. For this computation, the diffusion coefficients  $\mu$  and  $\kappa$  contain molecular and turbulent parts. The turbulent contributions are supplied through either algebraic or a two-equation  $k-\epsilon$  turbulence model.

The velocities in the  $\xi$ ,  $\eta$ , and  $\zeta$  coordinate directions can be written

$$\begin{aligned} U &= \xi_x + u\xi_x + v\xi_y + w\xi_z \\ V &= \eta_x + u\eta_x + v\eta_y + w\eta_z \\ W &= \zeta_x + u\zeta_x + v\zeta_y + w\zeta_z \end{aligned}$$

which represent the contravariant velocity components.

The Cartesian velocity components ( $u, v, w$ ) are retained as the dependent variables and are nondimensionalized with respect to  $a_\infty$  (the free stream speed of sound). The local pressure is determined using the relation

$$p = (\gamma - 1) [e - 0.5\rho(u^2 + v^2 + w^2)] \quad (4)$$

in which  $\gamma$  is the ratio of specific heats. Density,  $\rho$ , is referenced to  $\rho_\infty$  and the total energy,  $e$ , to  $\rho_\infty a_\infty^2$ . The transport coefficients are also nondimensionalized with respect to the corresponding free stream variables. Thus, the Prandtl number that appears in  $\hat{S}$  is defined as  $Pr = c_{p,\infty}\mu_\infty/\kappa_\infty$ . In differencing these equations, it is often advantageous to difference about a known base solution denoted by subscript 0 as

$$\begin{aligned} \delta_\tau(\hat{Q} - \hat{Q}_0) + \delta_\xi(\hat{F} - \hat{F}_0) + \delta_\eta(\hat{G} - \hat{G}_0) + \delta_\zeta(\hat{H} - \hat{H}_0) - Re^{-1}\delta_\zeta(\hat{S} - \hat{S}_0) \\ = -\partial_\tau\hat{Q}_0 - \partial_\xi\hat{F}_0 - \partial_\eta\hat{G}_0 - \partial_\zeta\hat{H}_0 + Re^{-1}\partial_\zeta\hat{S}_0 \end{aligned} \quad (5)$$

in which  $\delta$  indicates a general difference operator, and  $\partial$  is the differential operator. If the base state can be properly chosen, the differenced quantities can have smaller and smoother variation and therefore less of a differencing error (Pulliam and Steger 1982).

**2.2 Numerical Technique.** The implicit, approximately factored scheme for the thin layer Navier-Stokes equations using central differencing in the  $\eta$  and  $\zeta$  directions and upwinding in  $\xi$  is written in the following form

$$\begin{aligned} \left[ I + h\delta_\xi^b(\hat{A}^+)^n + h\delta_\zeta\hat{C}^n - hRe^{-1}\bar{\delta}_\zeta J^{-1}\hat{M}^n J - D_i|_\zeta \right] \\ \times [I + h\delta_\xi^f(\hat{A}^-)^n + h\delta_\eta\hat{B}^n - D_i|_\eta] \Delta\hat{Q}^n \\ = -\Delta t \{ \delta_\xi^b[(\hat{F}^+)^n - \hat{F}_\infty^+] + \delta_\xi^f[(\hat{F}^-)^n - \hat{F}_\infty^-] + \delta_\eta(\hat{G}^n - \hat{G}_\infty) \\ + \delta_\zeta(\hat{H}^n - \hat{H}_\infty) - Re^{-1}\bar{\delta}_\zeta(\hat{S}^n - \hat{S}_\infty) \} - D_e(\hat{Q}^n - \hat{Q}_\infty) \end{aligned} \quad (6)$$

in which  $h = \Delta t$  or  $(\Delta t)/2$  and the free stream base solution is used. Here,  $\delta$  is typically a three point second order accurate central difference operator,  $\bar{\delta}$  is a midpoint operator used with the viscous terms, and the operators  $\delta_{\xi}^b$  and  $\delta_{\xi}^f$  are backward and forward three-point difference operators. The flux  $\hat{F}$  has been eigensplit and the matrices  $\hat{A}$ ,  $\hat{B}$ ,  $\hat{C}$ , and  $\hat{M}$  result from local linearization of the fluxes about the previous time level. Here  $J$  denotes the Jacobian of the coordinate transformation. Dissipation operators  $D_e$  and  $D_i$  are used in the central space differencing directions. The smoothing terms used in the present study are of the form:

$$D_e|_{\eta} = (\Delta t)J^{-1} \left[ \epsilon_2 \bar{\delta} \rho(B) \beta \bar{\delta} + \epsilon_4 \bar{\delta} \frac{\rho(B)}{1+\beta} \bar{\delta}^3 \right] |_{\eta} J$$

$$D_i|_{\eta} = (\Delta t)J^{-1} \left[ \epsilon_2 \bar{\delta} \rho(B) \beta \bar{\delta} + 2.5 \epsilon_4 \bar{\delta} \rho(B) \bar{\delta} \right] |_{\eta} J$$

in which

$$\beta = \frac{|\bar{\delta}^2 P|}{|(1 + \bar{\delta}^2) P|}$$

and  $\rho(B)$  is the true spectral radius of  $B$ . The idea here is that the fourth difference will be tuned near shocks (e.g., as  $\beta$  gets large, the weight on the fourth difference drops down while the second difference tunes up).

For simplicity, most of the boundary conditions have been imposed explicitly (Sahu 1987). An adiabatic wall boundary condition is used on the body surface and the no-slip boundary condition is used at the wall. The pressure at the wall is calculated by solving a combined momentum equation. Free stream boundary conditions are used at the in-flow boundary as well as at the outer boundary. A symmetry boundary condition is imposed at the circumferential edges of the grid while a simple extrapolation is used at the downstream boundary. A combination of symmetry and extrapolation boundary condition is used at the center line (axis). Since the free stream flow is supersonic, a nonreflection boundary condition is used at the outer boundary. The flow field is initially set to free stream conditions everywhere and then advance in time until a steady state solution is obtained.

**2.3 Composite Grid Scheme.** In the present work, a simple composite grid scheme (Sahu 1990) has been used in which a large single grid is split into a number of smaller grids so that computations can be

performed on each grid separately. These grids use the available core memory one grid at a time. The remaining grids are stored on an external disk storage device such as the solid state disk device (SSD) of the Cray X-MP/48 computer. The Cray-2 has a large in-core memory to fit the large single grid. However, for accurate geometric modeling of complex projectile configurations, which include blunt noses, sharp corners, and base cavities, it is also desirable to split the large data base into a few smaller zones on the Cray-2 as well. The use of a composite grid scheme requires special care in storing and fetching the interface boundary data (i.e., the communication among the various zones). In the present scheme, there is a one to one mapping of the grid points at the interface boundaries. Thus, no interpolations are required. Details of the data storage, data transfer, and other pertinent information such as metric and differencing accuracy at the interfaces are given in the work of Sahu and Steger (1987) and Sahu (1988).

**2.4 Turbulence Modeling.** For the base flow calculations, three turbulence models have been used. Two of these are algebraic eddy viscosity models (Baldwin-Lomax model and Chow model). The third one is a two-equation k- $\epsilon$  turbulence model which is also an eddy viscosity model.

**2.4.1 Baldwin-Lomax Model.** This model is the one developed by Baldwin and Lomax (1978). It is a two-layer model in which an eddy viscosity is calculated for an inner and an outer region. The inner region follows the Prandtl-Van Driest formulation. In both the inner and outer formulations, the distribution of vorticity is used to determine the length scales, thereby avoiding the necessity of finding the outer edge of the boundary layer. For the inner region,

$$(\mu_t)_{inner} = \rho \ell^2 |\omega| \quad (7)$$

in which

$$\ell = \kappa y [1 - \exp(-y^+/A^+)]$$

$$y^+ = (\rho_w \mu_t y) / \mu_w, \quad \mu_t = \sqrt{(\tau_w / \rho_w)}$$

and  $|\omega|$  is the absolute magnitude of vorticity. The eddy viscosity for the outer region is given by

$$(\mu_t)_{outer} = KC_{cp} \rho F_{wake} F_{kleb}(y) \quad (8)$$

in which  $F_{wake} = y_{max} F_{max}$  or  $C_{wk} y_{max} u_{dif}^2 / F_{max}$ , the smaller of the two values. The quantities  $y_{max}$  and  $F_{max}$  are determined from the function  $F(y) = y|\omega|[1 - \exp(-y^+ / A^+)]$ , in which  $F_{max}$  is the maximum value of  $F(y)$  and  $y_{max}$  is the value of  $y$  at which it occurs. The function  $F_{kleb}^{(y)}$  is the Klebanoff intermittency factor. The quantity  $u_{dif}$  is the difference between the maximum and minimum total velocity in the profile and, for boundary layers, the minimum is zero.

The outer formulation can be used in wakes as well as in attached and separated boundary layers. For free shear layer flow regions or wakes, the Van Driest damping term  $[\exp(-y^+ / A^+)]$  is neglected. Also, for the base or wake region, the distance  $y$  is measured from the center line of symmetry. It is necessary to specify the following constants:  $A^+ = 26$ ,  $C_{cp} = 1.6$ ,  $C_{kleb} = 0.3$ ,  $C_{wk} = 0.25$ ,  $\kappa = 0.4$ , and  $K = 0.0168$ . This type of simple model is generally inadequate for complex flows containing flow separation regions such as base flow.

**2.4.2 Chow Model.** Another algebraic model that has been used in some of our base flow computations is that of Chow (1985). This model is intended to be used in the base or wake region only. It is based on the simple exchange-coefficient concept. The turbulent eddy viscosity coefficient is usually given by

$$\mu_t = \frac{1}{4\sigma^2} x u_e \quad (9)$$

in which  $x$  is the distance measured from the origin of the mixing region (i.e., the base),  $u_e$  is the velocity at the edge of the mixing region, and  $\sigma$  is the spread rate parameter. It is known that  $\sigma$  assumes a value of 12 for incompressible flow and it increases slightly with Mach number.

$$\sigma = 12 + 2.76 Me$$

in which  $Me$  is given by

$$Me^2 = \frac{2}{\gamma - 1} \left( \frac{1 + \frac{\gamma - 1}{2} M_\infty^2}{\left( \frac{\bar{P}_b}{P_\infty} \right)^{\frac{\gamma - 1}{\gamma}}} - 1 \right)$$



and  $\bar{P}_b/P_\infty$  is the average base pressure. The equivalent velocity  $u_e$  at the edge of the mixing region can be ascertained from

$$U_e = M_\infty \sqrt{\left(1 + \frac{\gamma-1}{2} M_\infty^2\right) / \left(1 + \frac{\gamma-1}{2} M_e^2\right)}$$

As a first approximation, the average value of  $\mu_t$  is assumed to be same at all points for a constant  $x$  location. After reattachment, turbulence should decay. Since the interest in the base flow calculations is to obtain the correct base pressure, it is assumed that the eddy viscosity level at the reattachment stays the same at other locations downstream. For base flow with jet, similar algebraic relations can be used for the jet shear layer. This model as well as Baldwin-Lomax (1978) model are algebraic models and depend only on local information. The two-equation model contains less empiricism and allows the flow history to be taken into account.

**2.4.3 Two-Equation k- $\epsilon$  Model.** The two-equation turbulence model used here is Chien's (1982) k- $\epsilon$  model which is similar to that of Jones and Launder (1972). In this model, two transport equations are solved for the two variables,  $k$  (turbulent kinetic energy) and  $\epsilon$  (turbulent dissipation rate).

$$\begin{aligned} \rho \frac{Dk}{Dt} = & \frac{\partial}{\partial X_j} \left[ \left( \frac{\mu_t}{\sigma_k} + \mu \right) \frac{\partial k}{\partial X_j} \right] + \mu_t \frac{\partial u_i}{\partial X_j} \left( \frac{\partial u_i}{\partial X_j} + \frac{\partial u_j}{\partial X_i} \right) \\ & - \rho \epsilon - 2\mu \frac{k}{y_n^2} \end{aligned} \quad (10)$$

$$\begin{aligned} \rho \frac{D\epsilon}{Dt} = & \frac{\partial}{\partial X_j} \left[ \left( \frac{\mu_t}{\sigma_\epsilon} + \mu \right) \frac{\partial \epsilon}{\partial X_j} \right] + c_1 \mu_t \frac{\epsilon}{k} \frac{\partial u_i}{\partial X_j} \left( \frac{\partial u_i}{\partial X_j} + \frac{\partial u_j}{\partial X_i} \right) \\ & - c_2 \rho \frac{\epsilon^2}{k} - 2\mu \frac{\epsilon}{y_n^2} e^{-\gamma^*/2} \end{aligned} \quad (11)$$

Here,  $y_n$  is the distance normal to the surface. The coefficients in the  $k$  and  $\epsilon$  equations are given by

$$\begin{aligned} c_1 &= 1.44 & c_3 &= 2.0, \quad \sigma_k = 1.0, \quad \sigma_\epsilon = 1.3 \\ c_2 &= 1.92 [1 - 0.3 \exp(-R_t^2)] & c_p &= 0.09 [1 - \exp(-0.01 y^+)] \end{aligned}$$

in which  $R_t = k^2/\nu \epsilon$ .

The  $k$ - $\epsilon$  model employs the eddy viscosity concept and relates the turbulent eddy viscosity to  $k$  and  $\epsilon$  by,

$$\mu_t = c_p \rho (k^2/\epsilon). \quad (12)$$

Following the same procedure used for the mean flow equations, the turbulence field equations can be written in conservation form and then transformed into generalized coordinates (Sahu and Danberg 1986).

The resulting axisymmetric set of transformed turbulence equations can be written as

$$\frac{\partial q_i}{\partial \tau} + \frac{\partial \hat{E}_i}{\partial \xi} + \frac{\partial \hat{G}_i}{\partial \zeta} = \frac{1}{Re} \left( \frac{\partial \hat{H}_i}{\partial \zeta} + \frac{\partial \hat{I}_i}{\partial \xi} + \hat{S}_i \right) \quad (13)$$

in which

$$\begin{aligned} q_i &= \frac{1}{J} \begin{bmatrix} \rho k \\ \rho \epsilon \end{bmatrix} \\ \hat{E}_i &= \frac{1}{J} \begin{bmatrix} \rho k U \\ \rho \epsilon U \end{bmatrix}, \quad \hat{G}_i = \frac{1}{J} \begin{bmatrix} \rho k W \\ \rho \epsilon W \end{bmatrix} \\ \hat{H}_i &= \frac{1}{J} \begin{bmatrix} (\zeta_x^2 + \zeta_y^2 + \zeta_z^2) \left( \frac{\mu_t}{\sigma_k} + \mu \right) \frac{\partial k}{\partial \zeta} \\ (\zeta_x^2 + \zeta_y^2 + \zeta_z^2) \left( \frac{\mu_t}{\sigma_\epsilon} + \mu \right) \frac{\partial \epsilon}{\partial \zeta} \end{bmatrix}, \quad \hat{I}_i = \frac{1}{J} \begin{bmatrix} (\xi_x^2 + \xi_y^2 + \xi_z^2) \left( \frac{\mu_t}{\sigma_k} + \mu \right) \frac{\partial k}{\partial \xi} \\ (\xi_x^2 + \xi_y^2 + \xi_z^2) \left( \frac{\mu_t}{\sigma_\epsilon} + \mu \right) \frac{\partial \epsilon}{\partial \xi} \end{bmatrix} \\ \hat{S}_i &= \frac{1}{J} \begin{bmatrix} P - \rho \epsilon Re - 2\mu \frac{k}{y_n^2} \\ c_1 \frac{\epsilon}{k} P - C_2 \rho \frac{\epsilon^2}{K} Re - 2\mu \frac{\epsilon}{y_n^2} \exp(-y^+/2) \end{bmatrix}, \end{aligned}$$

and  $P$  is the production term given as

$$P = \mu_t (\zeta_x^2 + \zeta_y^2 + \zeta_z^2) (u_\zeta^2 + v_\zeta^2 + w_\zeta^2) + \mu_t (\zeta_x u_\zeta + \zeta_y v_\zeta + \zeta_z w_\zeta)^2 \\ + \mu_t (\xi_x^2 + \xi_y^2 + \xi_z^2) (u_\xi^2 + v_\xi^2 + w_\xi^2) + \mu_t (\xi_x u_\xi + \xi_y v_\xi + \xi_z w_\xi)^2$$

This constitutes a low Reynolds number formulation of the k- $\epsilon$  model. Calculations are extended to the wall itself, and exact values of the dependent variables at the wall are used as boundary conditions. Chien's model is better mathematically behaved near the wall and is, thus, used in this study.

The turbulence field equations are solved using the Beam and Warming (1978), implicit, approximately factored, finite difference scheme. A convenient solution algorithm for these equations has the following sequence:

$$[(I - \Delta t D^n) + \Delta t (\delta_\zeta B^n - \delta_\zeta C^n)] \Delta q_i^n = RHS \quad (13) \quad (14a)$$

$$[I + \Delta t (\delta_\xi A^n - \delta_\xi N^n)] \Delta q_i^n = \Delta q_i^n \quad (14b)$$

$$q_i^{n+1} = q_i^n + \Delta q_i^n \quad (14c)$$

in which  $RHS$  is the right-hand side of Equation 13.  $A$  and  $B$  are Jacobian matrices resulting from the local linearization of the flux terms  $\hat{E}_i$  and  $\hat{G}_i$ . The source terms are treated implicitly. This results in the Jacobian matrices  $C$ ,  $N$ , and  $D$ , which are included in the  $\zeta$  and  $\xi$  operators as shown in Equation 14. The Jacobian matrices are given as

$$A = \begin{bmatrix} U & 0 \\ 0 & U \end{bmatrix} \quad B = \begin{bmatrix} W & 0 \\ 0 & W \end{bmatrix} \\ C = \begin{bmatrix} \alpha_k \frac{\partial}{\partial \zeta} \left( \frac{J}{\rho} \right) & 0 \\ 0 & \alpha_\epsilon \frac{\partial}{\partial \zeta} \left( \frac{J}{\rho} \right) \end{bmatrix}, \quad N = \begin{bmatrix} \alpha_k \frac{\partial}{\partial \xi} \left( \frac{J}{\rho} \right) & 0 \\ 0 & \alpha_\epsilon \frac{\partial}{\partial \xi} \left( \frac{J}{\rho} \right) \end{bmatrix} \\ D = \begin{bmatrix} \left( 2C_p \frac{k}{\epsilon} - Re^{-1} \frac{2\mu}{\rho y_n^2} \right) \left( -C_p \frac{\kappa^2}{\epsilon^2} P - 1 \right) \\ \left( c_1 C_p P + c_2 \frac{\epsilon^2}{k^2} \right) \left( -2c_2 \frac{\epsilon}{k} - Re^{-1} \frac{2\mu}{\rho y_n^2} \exp^{-y^+/2} \right) \end{bmatrix}$$

in which

$$\alpha = \frac{Re^{-1}}{J} \left( \frac{\mu_i}{\sigma} + \mu \right) (\zeta_x^2 + \zeta_y^2 + \zeta_z^2).$$

The operators  $\delta_x$  and  $\delta_z$  are central difference operators. The numerical smoothing is based on an up-wind scheme, and the details are given in Sahu (1984).

### 3. MODEL GEOMETRY AND EXPERIMENT

The computational accuracy of a numerical scheme can be established through comparisons with available experimental data. The model used in the experiment and in the computational study is shown in Figure 2. It is an axisymmetrical cylindrical afterbody, which has a diameter of 63.5 mm. This figure also shows the stations where mean and fluctuating velocity components were measured with a Laser Doppler Velocimeter (LDV) system. The same configuration is used in the numerical simulations for a direct comparison.

Experimental measurements (Herrin and Dutton 1991) for this model have been made at the University of Illinois supersonic wind tunnel. The model was tested at  $0^\circ$  angle of attack, Mach number of 2.46, and Reynolds number of  $5.21 \times 10^7$  per meter. In addition to measuring the velocity components at a few selected longitudinal positions in the wake or base region, the base pressure was measured at 19 positions along the base. Such detailed base pressure measurements have not been made in the past and are very helpful in the code validation process. The velocity profile is also measured at a station upstream from the base, which provides the upstream boundary condition for base region flow field calculations.

### 4. RESULTS

Numerical computations have been made for the cylindrical afterbody at a Mach number 2.46 and at  $0^\circ$  angle of attack. The three-plane version of the 3D code was run for the  $0^\circ$  angle of attack case. Two end planes were used to specify symmetrical boundary conditions in the circumferential plane.

The solution technique requires the discretization of the entire flow region of interest into a suitable computational grid. The grid outer boundary has been placed 1 diameter away from the surface of the afterbody. The downstream boundary was placed 10 diameters away from the base. Since the calculations

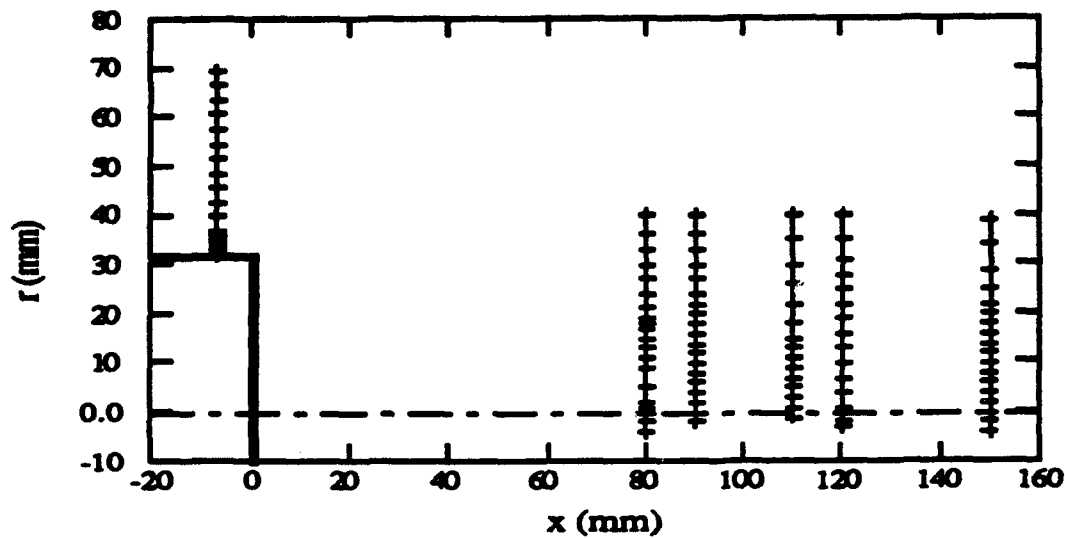


Figure 2. Afterbody Measurement Locations.

are in the supersonic regime, the computational outer boundary was placed close to the body and a no reflection boundary condition used at that boundary. Figure 3 shows an expanded view of the grid in the base region. The surface points on the afterbody and the base were obtained first. These were then used as inputs for obtaining the full grid using an algebraic grid generation program. The full grid is split into two zones, one upstream from the base, and the other one in the base region or the wake. These grids consist of  $22 \times 60$  and  $95 \times 119$  grid points, respectively. Figure 3 shows the longitudinal grid clustering near the base corner. Grid points are also clustered near the afterbody surface to capture the viscous effects in the turbulent boundary layer. These clustered grid points are spread out downstream of the base in the wake to capture the free shear layer region. For the  $0^\circ$  angle of attack case considered, the grid was rotated circumferentially  $5^\circ$  on either side of the midplane. This provided the three planes needed in the code to use central finite differences in the circumferential direction. In each case, the solution was marched from free stream conditions everywhere until the final converged solution was obtained. The results are now presented for both mean and turbulence quantities. Comparison of the computed results is made with the available experimental data (Herrin and Dutton 1991).

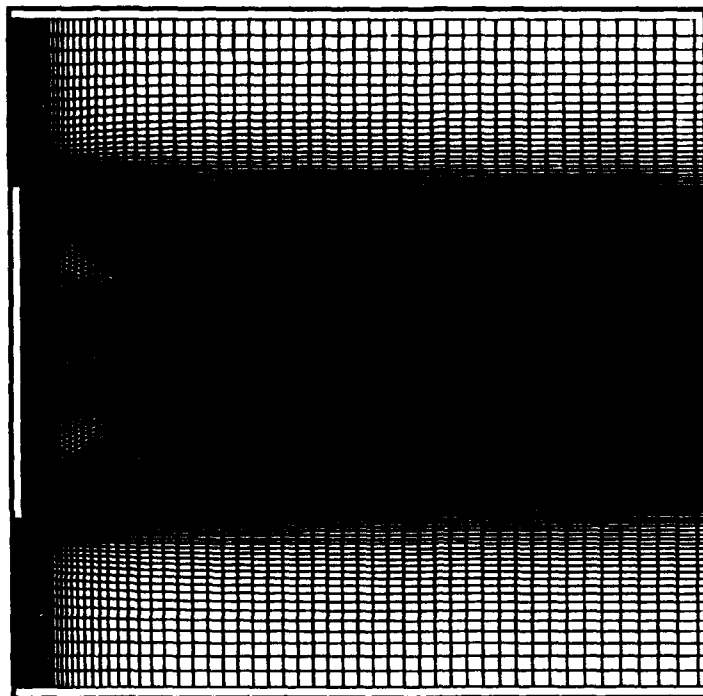


Figure 3. Base Region Computational Grid.

A few qualitative results are presented next. Figure 4 shows the pressure contour plot for the base region. The features to observe are the flow expansion at the base corner followed by the recompression shock downstream from the base (coalescence of contour lines). Figures 5a and 5b show the comparison of the computed Mach number contours with experimentally obtained Schlieren photograph of the base region flow field. Both the experiment and the computed results show the flow expansion at the base and the recompression shock downstream from the base. In addition, Figures 5a and 5b show the free shear layer in the near wake. Although not indicated in Figure 5a, the flow in the near wake is primarily subsonic. Figure 6 shows the computed velocity vectors in the base region. The recirculatory flow in the near wake is clearly evident. Flow reattachment occurs at about three base radii downstream from the base. The magnitude of the velocity is shown to be quite small in the immediate vicinity of the base. The computed results shown in Figures 4, 5, and 6 were obtained using the two-equation  $k-\epsilon$  model.

Figures 7 and 8 show the velocity components in the stream-wise and normal directions, respectively. These velocity profiles are taken at four longitudinal positions in the wake or the base region ( $X/D = 1.26, 1.42, 1.73, \text{ and } 1.89$ ). The computed velocity profiles obtained using two algebraic turbulence models and the two-equation  $k-\epsilon$  model are compared with the experimental data. Figure 7 shows the comparison of

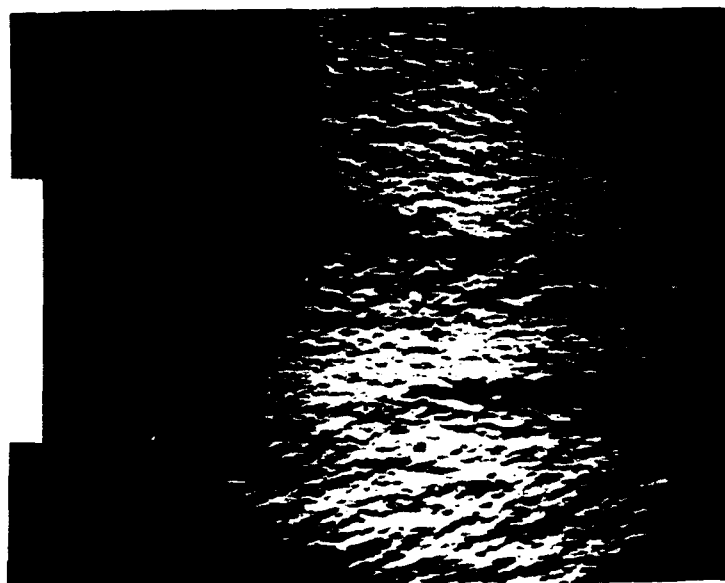


Figure 4. Computed Pressure Contours in the Base Region,  $M_{\infty} = 2.46$ ,  $\alpha = 0$ , and k- $\epsilon$  Model.

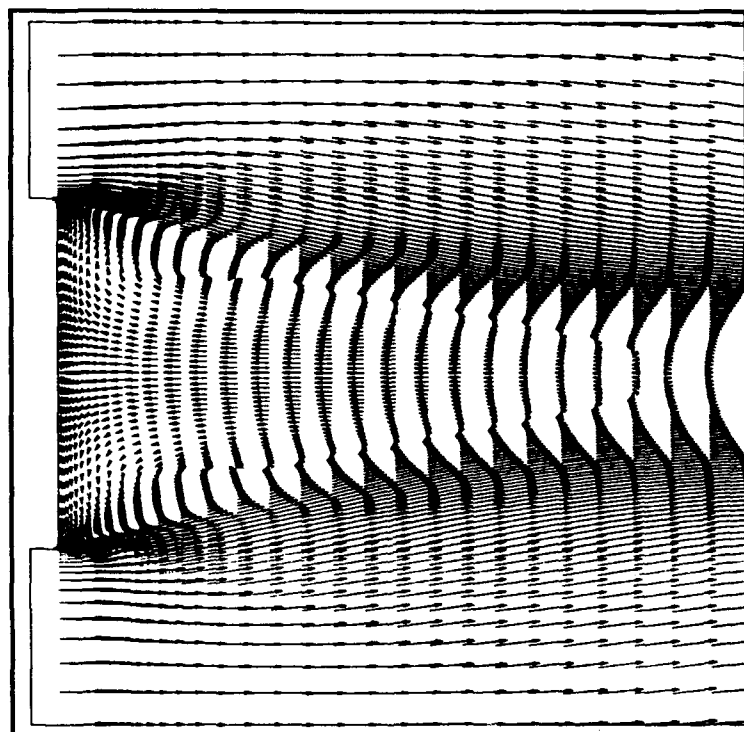


Figure 5a. Computed Mach Contours,  $M_{\infty} = 2.46$ ,  $\alpha = 0$ , and k- $\epsilon$  Model.

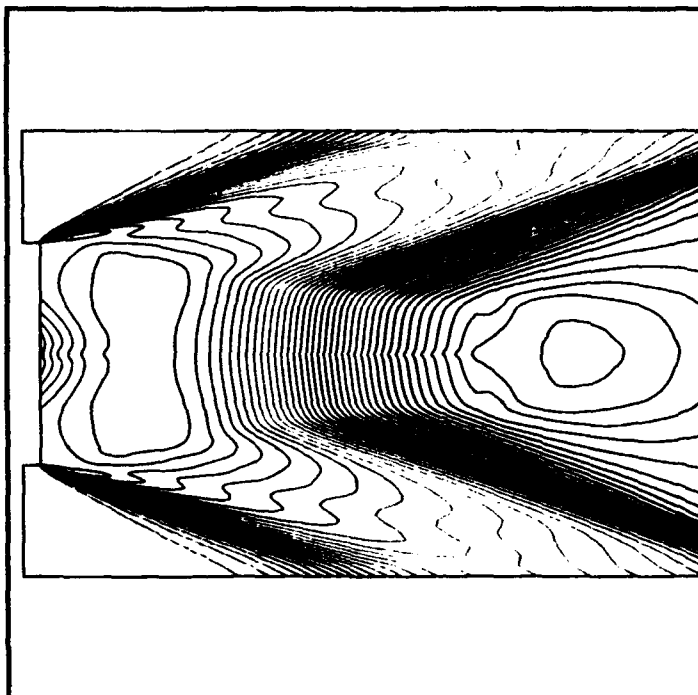


Figure 5b. Experimental Schlieren Photograph.

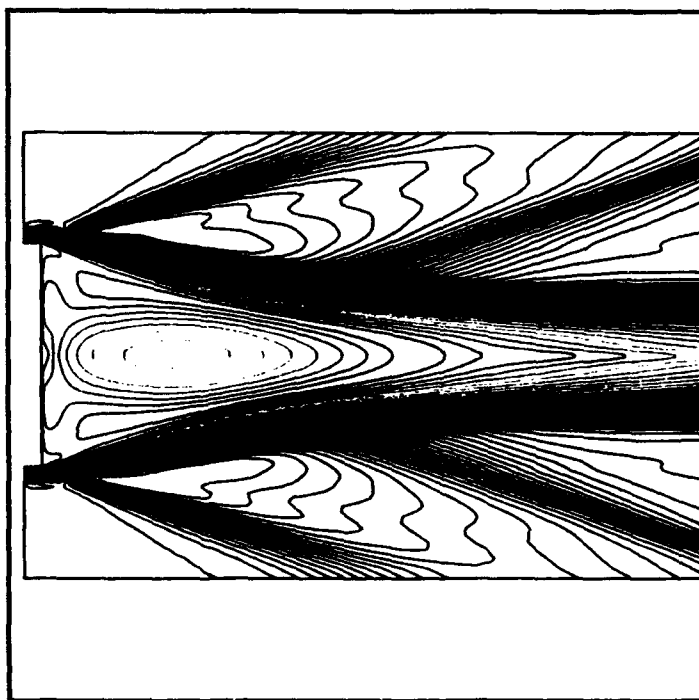


Figure 6. Velocity Vectors in the Base Region,  $M_{\infty} = 2.46$ ,  $\alpha = 0$ , and k- $\epsilon$  Model.



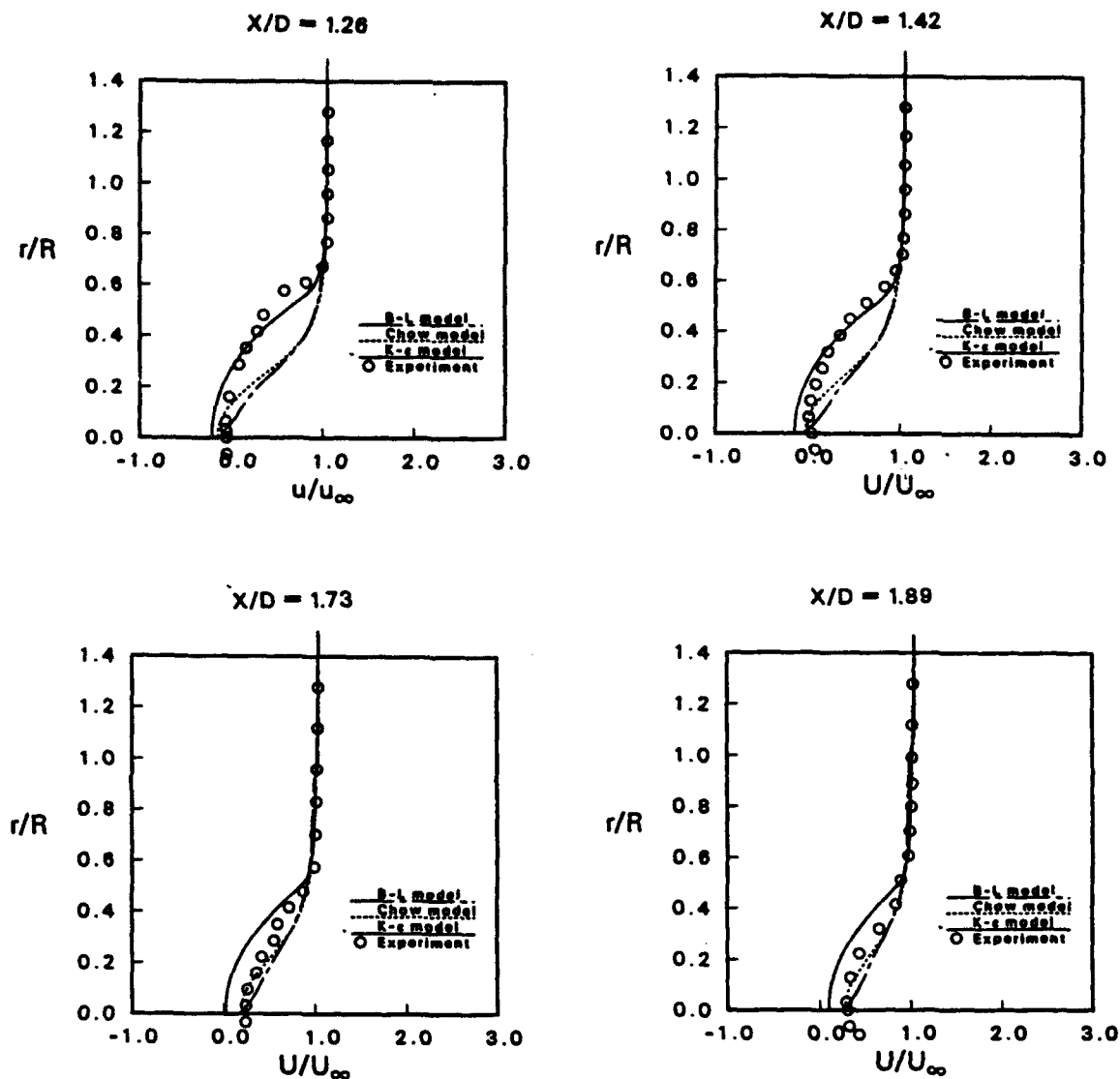


Figure 7. Stream-wise Velocity ( $u$ ) Profiles,  $M_\infty = 2.46$ ,  $\alpha = 0$ .

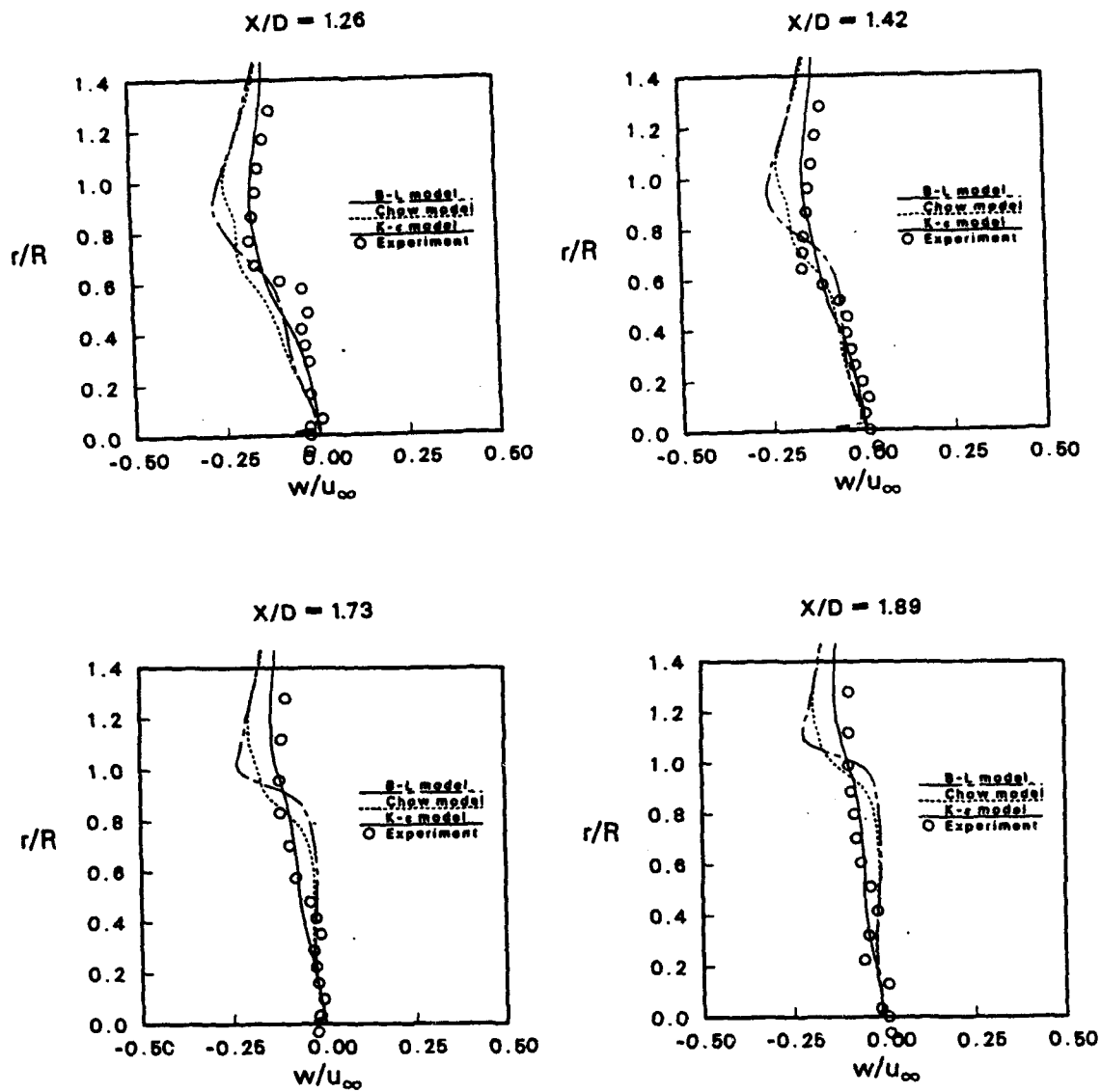


Figure 8. Normal Velocity ( $w$ ) Profiles,  $M_\infty = 2.46$ ,  $\alpha = 0$ .

the  $u$  (stream-wise) component of velocity. In general, the profiles obtained with the  $k-\epsilon$  model agree much better with the experiment in the shear layer regions for  $X/D = 1.26$  and  $X/D = 1.42$ . The profiles are rather poorly predicted by both the algebraic models at these two stations. The reattachment point estimated from the experimental measurements is about 1.4 base diameters downstream from the base. The computed value with the  $k-\epsilon$  model is 1.5. This small disagreement is also seen in the flow redevelopment region downstream from the reattachment ( $X/D = 1.73$  and  $1.89$ ). The algebraic turbulence models predict the reattachment point better than that predicted by the  $k-\epsilon$  model. The velocity profiles predicted with these models agree fairly well with the experimentally obtained profiles at these two stations. Chow model predictions are slightly better than those predicted by the Baldwin-Lomax model in this flow redevelopment region. Figure 8 shows the comparison of the  $w$  (vertical) component of the velocity. This component of velocity is better predicted by the  $k-\epsilon$  model than the algebraic models both in the flow recirculation and redevelopment regions. The profiles by the algebraic models do not agree well with the experimental data for radial positions greater than half of the base radius.

Some of the turbulence quantities are presented next. Figure 9 shows the turbulent kinetic energy profiles at the same longitudinal positions in the wake. The computed  $k$  profiles are obtained using the two-equation  $k-\epsilon$  turbulence model. In the recirculation region ( $X/D = 1.26$ ) and near the reattachment ( $X/D = 1.42$ ), the peak observed experimentally ( $r/R = 0.5$ ) is poorly predicted by the  $k-\epsilon$  model ( $r/R = 0.4$ ). The location and the magnitude of the peak agree somewhat better at  $X/D = 1.42$  than at  $X/D = 1.26$ . The agreement of the computed profiles with the data is good in the flow redevelopment region ( $X/D = 1.73$  and  $1.89$ ). Figure 10 shows the turbulent dissipation rate ( $\epsilon$ ) profiles at the same positions in the wake. As seen in this figure,  $\epsilon$  increases from the center line of symmetry with radius to about 0.4 of the base height where the peaks occur and then drops quickly to very small values at about  $r/R = 0.65$ . The magnitude and the location of the peaks decrease smoothly with increasing axial distances downstream from the base.

Figure 11 shows the turbulent shear stress profiles in the wake. The computed values obtained by both the algebraic models and the  $k-\epsilon$  model are compared with the experimental data. In general, a small improvement can be observed in the predicted values with the  $k-\epsilon$  model over the algebraic models. Discrepancy exists between the experimentally obtained turbulent shear stress and the predicted shear stresses with all the turbulence models. This is true especially near the peaks at  $X/D = 1.26$  and  $1.42$ . The magnitude of the peak predicted by the  $k-\epsilon$  model is about the same as predicted by the Baldwin-Lomax model at these two positions; however, they both underpredict the experimental peak. The Chow

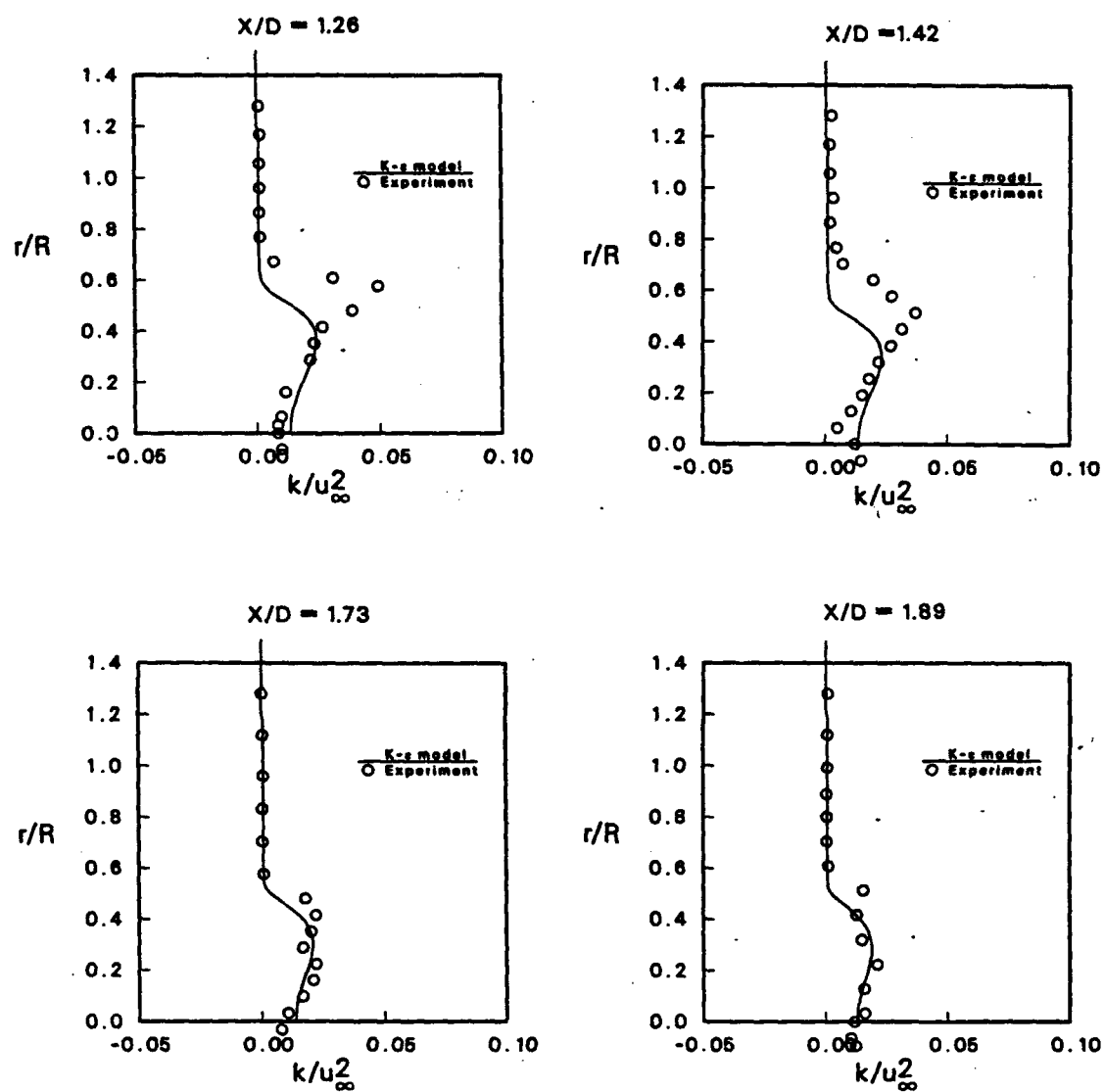


Figure 9. Turbulent Kinetic Energy Profiles,  $M_\infty = 2.46$ ,  $\alpha = 0$ .

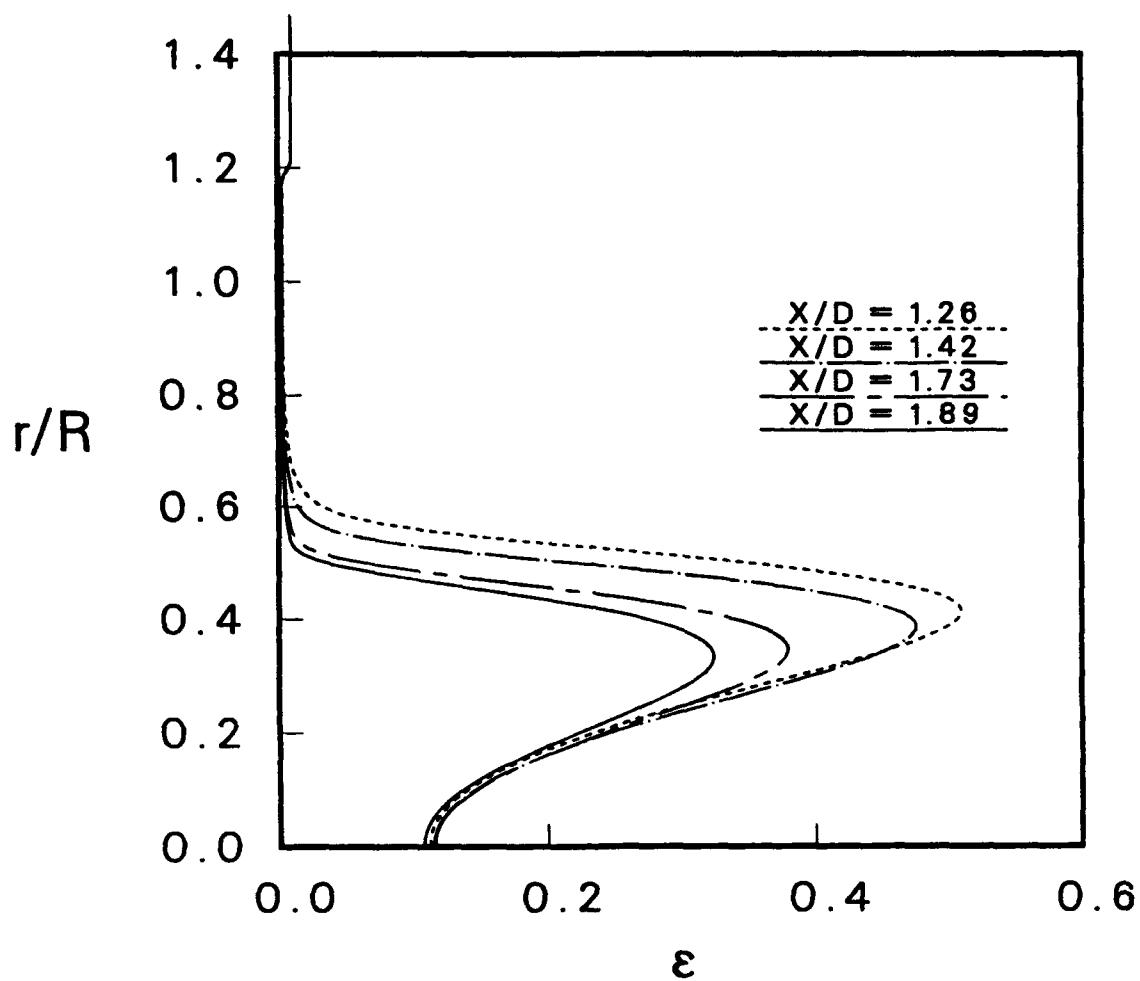


Figure 10. Turbulent Dissipation Rate Profiles,  $M_{\infty} = 2.46$ ,  $\alpha = 0$ .

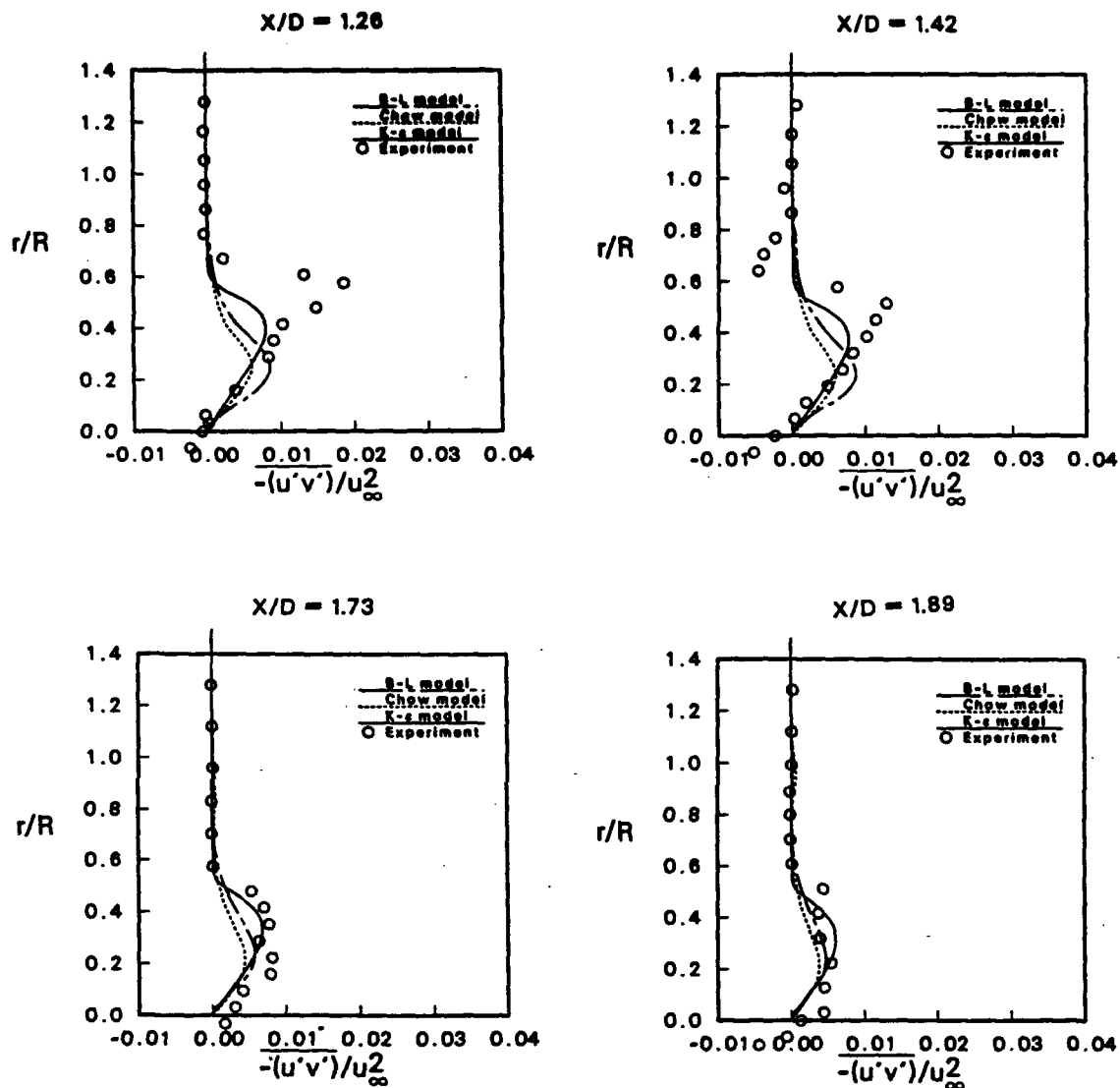


Figure 11. Turbulent Shear Stress Profiles,  $M_\infty = 2.46$ ,  $\alpha = 0$ .

model underpredicts the peak even more. As for the location of the peak, the k- $\epsilon$  model does better than the algebraic models. As  $X/D$  is increased from 1.26 to 1.42, the location of the peak predicted by the k- $\epsilon$  model moves closer to the center line similar to that observed in the experiment. This is not seen in the prediction by the algebraic models. The k- $\epsilon$  model predictions agree better than the predictions by the algebraic models at  $X/D = 1.73$  and 1.89.

Of particular interest is the accurate prediction or determination of base pressure and, hence, base drag. Figure 12 shows the base pressure distribution (along the base). The base pressures predicted by both the algebraic models and the two-equation k- $\epsilon$  turbulence model are compared with the experimental data (Herrin and Dutton 1991). The experimental data are shown in dark circles, and the computed results are shown in lines. Here,  $Z/D = 0.0$  corresponds to the center line of symmetry and  $Z/D = 0.5$  corresponds to the base corner. The base pressures predicted by both algebraic turbulence models show a big increase near the center line of symmetry. The experimental data show almost no change (only 3%) in the base pressure distribution. The base pressures are very poorly predicted by the algebraic models, not only near the center line but also near the base corner. A much improved base pressure distribution is predicted by the k- $\epsilon$  model, and its agreement with the measured base pressure is quite good. The k- $\epsilon$  prediction shows a small increase in the base pressure near the center line, which is not observed in the data.

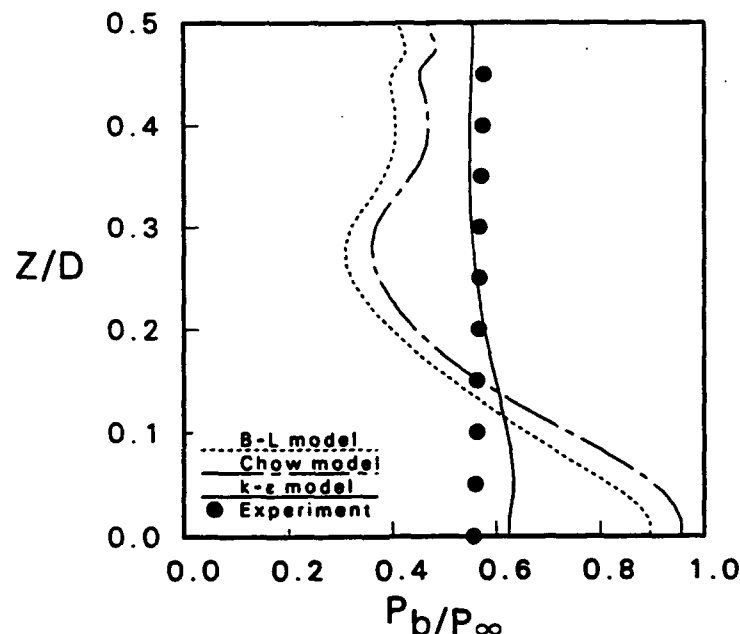


Figure 12. Base Pressure Distribution,  $M_\infty = 2.46$ ,  $\alpha = 0$ .

## 5. CONCLUDING REMARKS

A zonal, implicit, time-marching Navier-Stokes computational technique has been used to compute the turbulent supersonic base flow over a cylindrical afterbody. Flow field computations have been performed at  $M_\infty = 2.46$  and at the angle of attack,  $\alpha = 0.0$ . Various eddy viscosity turbulence models (two algebraic and a two-equation k- $\epsilon$ ) have been used to provide the turbulence closure. The k- $\epsilon$  equations were formulated in a generalized coordinate system and were solved using an implicit algorithm.

Numerical results show the details of the flow field such as Mach number contours, pressure contours, and velocity vector plots. Comparison of both the mean and turbulence quantities has been made with the available experimental data. Both algebraic turbulence models predict the mean velocity components poorly in the recirculatory flow region in the wake. In general, the velocity components predicted by the two-equation k- $\epsilon$  model agree better with the experimental data than the algebraic models do. Discrepancy exists between the predicted turbulent shear stress and the experiment for all these turbulence models. A small improvement in the predicted location and magnitude of the peak in shear stress exists with the k- $\epsilon$  model. Computed base pressure distributions have been compared with the measured base pressures. The base pressures predicted by the algebraic models show a much larger variation and do not agree well with the data, compared to the k- $\epsilon$  model. The measured base pressures show a very small change along the base and are predicted rather well with the k- $\epsilon$  turbulence model.



## 6. REFERENCES

- Baldwin, B. S., and H. Lomax. "Thin Layer Approximation and Algebraic Model for Separated Turbulent Flows." AIAA Paper No. 78-257, January 1978.
- Beam, R., and R. F. Warming. "An Implicit Factored Scheme for the Compressible Navier-Stokes Equations." AIAA Journal, vol. 16, pp. 393-402, April 1978.
- Chien, K. Y. "Predictions of Channel and Boundary-Layer Flows with a Low-Reynolds-Number Turbulence Model." AIAA Journal, vol. 20, pp. 33-38, January 1982.
- Chow, W. L. "Improvement on Numerical Computation of the Thin-Layer Navier-Stokes Equation—With Special Emphasis on the Turbulent Base Pressure of a Projectile in Transonic Flight Condition." Contract Report No. DAAG29-81-D-0100, University of Illinois, Urbana-Champaign, Urbana, IL, November 1985.
- Herrin, J. L., and J. C. Dutton. "An Experimental Investigation of the Supersonic Axisymmetric Base Flow behind a Cylindrical Afterbody." UILU 91-4004, University of Illinois at Urbana-Champaign, Urbana, IL, May 1991.
- Jones, W. P., and B. E. Launder. "The Prediction of Laminarization With a Two-Equation Model of Turbulence." International Journal of Heat and Mass Transfer, vol. 15, 1972.
- Pulliam, T. H., and J. L. Steger. "On Implicit Finite-Difference Simulations of Three-Dimensional Flow." AIAA Journal, vol. 18, no. 2, pp. 159-167, February 1982.
- Sahu, J. "Navier-Stokes Computational Study of Axisymmetric Transonic Turbulent Flows with a Two-Equation Model of Turbulence." Ph.D. Dissertation, University of Delaware, Newark, DE, June 1984.
- Sahu, J. "Supersonic Base Flow Over Cylindrical Afterbodies With Base Bleed." AIAA Paper No. 86-0487, Proceedings of the 24th Annual Aerospace Sciences Meeting, Reno, NV, January 1986.
- Sahu, J. "Computations of Supersonic Flow Over a Missile Afterbody Containing an Exhaust Jet." AIAA Journal of Spacecraft and Rockets, vol. 24, no. 5, pp. 403-410, September-October 1987.
- Sahu, J. "Numerical Computations of Transonic Critical Aerodynamic Behavior." AIAA Journal, vol. 28, no. 5, pp. 807-816, May 1990. (also see BRL-TR-2962, December 1988)
- Sahu, J., and J. E. Danberg. "Navier-Stokes Computations of Transonic Flows with a Two-Equation Turbulence Model." AIAA Journal, vol. 24, no. 11, pp. 1744-1751, November 1986.
- Sahu, J., and C. J. Nietubicz. "Three Dimensional Flow Calculation for a Projectile With Standard and Dome Bases." BRL-TR-3150, U.S. Army Ballistic Research Laboratory, Aberdeen Proving Ground, MD, September 1990.

Sahu, J., C. J. Nietubicz, and J. L. Steger. "Navier-Stokes Computations of Projectile Base Flow With and Without Base Injection." BRL-TR-02532, U.S. Army Ballistic Research Laboratory, Aberdeen Proving Ground, MD, November 1983. (also see AIAA Journal, vol. 23, no. 9, pp. 1348-1355, September 1985)

Sahu, J., and J. L. Steger. "Numerical Simulation of Three-Dimensional Transonic Flows." AIAA Paper No. 87-2293, Atmospheric Flight Mechanics Conference, Monterey, CA, August 1987. (also see BRL-TR-2903, March 1988)

## LIST OF SYMBOLS

$a$	speed of sound
$A^+$	Van Driest's damping factor
$c_1, c_2, c_\mu$	empirical constants in the k- $\epsilon$ turbulence model
$c_p$	specific heat at constant pressure
$C_p$	pressure coefficient, $2(P - P_\infty)/\rho_\infty u_\infty^2$
$D$	body diameter
$e$	total energy per unit volume/ $\rho_\infty a_\infty^2$
$\hat{E}, \hat{F}, \hat{G}$	flux vector of transformed Navier-Stokes equations
$\hat{H}$	source term vector
$I$	identity matrix
$J$	Jacobian of the transformation
$k$	turbulent kinetic energy/ $a_\infty^2$
$l$	mixing length
$M$	Mach number
$p$	pressure/ $\rho_\infty a_\infty^2$
$Pr$	Prandtl number, $\mu_\infty c_p / \kappa_\infty$
$\hat{q}$	vector of dependent variables in transformed equations
$R$	base radius
$Re$	Reynolds number, $\rho_\infty a_\infty D / \mu_\infty$
$R_t$	turbulent Reynolds number, $k^2 / \nu \epsilon$
$\hat{S}$	viscous flux vector or source terms in the k- $\epsilon$ equations
$t$	physical time
$u, v, w$	Cartesian velocity components/ $a_\infty$
$U, V, W$	Contravariant velocities/ $a_\infty$
$u_\tau$	friction velocity, $\sqrt{\tau_w / \rho_w}$
$x, y, z$	physical Cartesian coordinates
$y^+$	law of the wall coordinate, $(\rho_w u_\tau y / \mu_w)$
$\alpha$	angle of attack
$\gamma$	ratio of specific heats
$\kappa$	coefficient of thermal conductivity/ $\kappa_\infty$
$\mu$	coefficient of viscosity/ $\mu_\infty$
$\xi, \eta, \zeta$	transformed coordinates in axial, circumferential and normal directions
$\rho$	density/ $\rho_\infty$
$\epsilon$	turbulent dissipation rate/ $(a_\infty^3 / D)$
$\tau$	transformed time
$\tau_w$	shear stress at the wall
$\nu$	kinematic viscosity, $\mu / \rho$

$\sigma_k, \sigma_\epsilon$  empirical constants in the k-e equations  
 $\omega$  vorticity

Superscript

\*

critical value

Subscript

t

turbulent

w

wall conditions

$\infty$

free stream conditions

<u>No. of Copies</u>	<u>Organization</u>	<u>No. of Copies</u>	<u>Organization</u>
2	Administrator Defense Technical Info Center ATTN: DTIC-DDA Cameron Station Alexandria, VA 22304-6145	1	Commander U.S. Army Missile Command ATTN: AMSMI-RD-CS-R (DOC) Redstone Arsenal, AL 35898-5010
1	Commander U.S. Army Materiel Command ATTN: AMCAM 5001 Eisenhower Ave. Alexandria, VA 22333-0001	1	Commander U.S. Army Tank-Automotive Command ATTN: AMSTA-JSK (Armor Eng. Br.) Warren, MI 48397-5000
1	Director U.S. Army Research Laboratory ATTN: AMSRL-OP-CI-AD, Tech Publishing 2800 Powder Mill Rd. Adelphi, MD 20783-1145	1	Director U.S. Army TRADOC Analysis Command ATTN: ATRC-WSR White Sands Missile Range, NM 88002-5502
1	Director U.S. Army Research Laboratory ATTN: AMSRL-OP-CI-AD, Records Management 2800 Powder Mill Rd. Adelphi, MD 20783-1145	(Class. only) 1	Commandant U.S. Army Infantry School ATTN: ATSH-CD (Security Mgr.) Fort Benning, GA 31905-5660
2	Commander U.S. Army Armament Research, Development, and Engineering Center ATTN: SMCAR-TDC Picatinny Arsenal, NJ 07806-5000	(Unclass. only) 1	Commandant U.S. Army Infantry School ATTN: ATSH-WCB-O Fort Benning, GA 31905-5000
1	Director Benet Weapons Laboratory U.S. Army Armament Research, Development, and Engineering Center ATTN: SMCAR-CCB-TL Watervliet, NY 12189-4050	1	WL/MNOI Eglin AFB, FL 32542-5000  <u>Aberdeen Proving Ground</u>
1	Director U.S. Army Advanced Systems Research and Analysis Office (ATCOM) ATTN: AMSAT-R-NR, M/S 219-1 Ames Research Center Moffett Field, CA 94035-1000	2	Dir, USAMSAA ATTN: AMXSY-D AMXSY-MP, H. Cohen
		1	Cdr, USATECOM ATTN: AMSTE-TC
		1	Dir, USAERDEC ATTN: SCBRD-RT
		1	Cdr, USACBDCOM ATTN: AMSCB-CII
		1	Dir, USARL ATTN: AMSRL-SL-I
		5	Dir, USARL ATTN: AMSRL-OP-AP-L

<u>No. of Copies</u>	<u>Organization</u>
1	HQDA (SARD-TR/Ms. K. Kominos) WASH DC 20310-0103
1	HQDA (SARD-TR/Dr. R. Chait) WASH DC 20310-0103
2	USAF Wright Aeronautical Laboratories ATTN: AFWAL/FIMG, Dr. J. Shang Mr. N. E. Scaggs WPAFB, OH 45433-6553
3	Commander Naval Surface Weapons Center ATTN: Code R44, Dr. F. Priolo Code R44, Dr. A. Wardlaw K24, B402-12, Dr. W. Yanta White Oak Laboratory Silver Spring, MD 20903-5000
4	Director National Aeronautics and Space Administration Langley Research Center ATTN: Tech Library Mr. D. M. Bushnell Dr. M. J. Hensch Dr. J. South Langley Station Hampton, VA 23665
2	Interferometrics, Inc. 8150 Leesburg Pike ATTN: Rene Larriva Eric L. Strobel Vienna, VA 22180
2	DARPA ATTN: Dr. P. Kemmey Dr. James Richardson 3701 North Fairfax Dr. Arlington, VA 22203-1714

<u>No. of Copies</u>	<u>Organization</u>
6	Director National Aeronautics and Space Administration Ames Research Center ATTN: MS-227-8, L. Schiff MS-258-1, T. Holst MS-258-1, D. Chaussee MS-258-1, M. Rai MS-258-1, P. Kutler MS-258-1, P. Buning Moffett Field, CA 94035
1	United States Military Academy Department of Mechanics ATTN: LTC Andrew L. Dull West Point, NY 10996
6	Commander U.S. Army Armament Research, Development, and Engineering Center ATTN: SMCAR-AET-A, R. DeKleine R. Kline R. Botticelli H. Hudgins J. Grau S. Kahn Picatinny Arsenal, NJ 07806-5001
1	Commander U.S. Army Armament Research, Development, and Engineering Center ATTN: SMCAR-CCH-V, Paul Valenti Picatinny Arsenal, NJ 07806-5001
1	Commander U.S. Naval Surface Weapons Center ATTN: Dr. F. Moore Dahlgren, VA 22448
3	University of California, Davis Department of Mechanical Engineering ATTN: Prof. H. A. Dwyer Prof. M. Hafez Dr. B. Meakin Davis, CA 95616

<u>No. of Copies</u>	<u>Organization</u>
3	Science and Technology Inc. 4001 North Fairfax Dr., No. 700 ATTN: Dr. Alan Glasser Mr. Bruce Lohman Mr. Dave Maurizi Arlington, VA 22203-1618
3	Air Force Armament Laboratory ATTN: AFATL/FXA, Stephen C. Korn Bruce Simpson Dave Belk Eglin AFB, FL 32542-5434
1	Massachusetts Institute of Technology ATTN: Tech Library 77 Massachusetts Ave. Cambridge, MA 02139
1	Grumman Aerospace Corporation Aerophysics Research Department ATTN: Dr. R. E. Melnik Bethpage, NY 11714
1	AEDC Calspan Field Service ATTN: MS 600, Dr. John Benek Tullahoma, TN 37389
1	Virginia Polytechnic Institute and State University ATTN: Dr. Clark H. Lewis Department of Aerospace and Ocean Engineering Blacksburg, VA 24061
1	Los Alamos National Laboratory ATTN: Mr. Bill Hogan MS G770 Los Alamos, NM 87545
3	Director Sandia National Laboratories ATTN: Div. 1554, Dr. W. Oberkampf Div. 1554, Dr. F. Blotner Div. 1636, Dr. W. Wolfe Albuquerque, NM 87185

<u>No. of Copies</u>	<u>Organization</u>
1	Advanced Technology Center Arvin/Calspan Aerodynamics Research Department ATTN: Dr. M. S. Holden P.O. Box 400 Buffalo, NY 14225
1	Pennsylvania State University Department of Aerospace Engineering ATTN: Dr. G. S. Dulikravich University Park, PA 16802
1	University of Illinois at Urbana Champaign Department of Mechanical and Industrial Engineering ATTN: Dr. J. C. Dutton Urbana, IL 61801
1	University of Maryland Department of Aerospace Engineering ATTN: Dr. J. D. Anderson, Jr. College Park, MD 20742
1	University of Notre Dame Department of Aeronautical and Mechanical Engineering ATTN: Prof. T. J. Mueller Notre Dame, IN 46556
1	University of Texas Department of Aerospace Engineering Mechanics ATTN: Dr. D. S. Dolling Austin, TX 78712-1055
1	University of Delaware Department of Mechanical Engineering ATTN: Dr. John Meakin, Chairman Newark, DE 19716
1	IAT ATTN: Curt Ober 4030-2 West Braker Lane Austin, TX 78759-5329

**No. of  
Copies    Organization**

- 1    University of Florida  
      Department of Engineering Sciences  
      College of Engineering  
      ATTN: Prof. C. C. Hsu  
      Gainesville, FL 32611

**Aberdeen Proving Ground**

- 25    Dir, USARL  
      ATTN: AMSRL-WT-P,  
            Mr. Albert Horst  
            AMSRL-WT-PB,  
            Dr. E. Schmidt  
            Dr. M. Bundy  
            Dr. K. Fansler  
            Mr. E. Ferry  
            Mr. B. Guidos  
            Mrs. K. Heavey  
            Mr. H. Edge  
            Mr. C. Nietubicz  
            Mr. V. Oskay  
            Dr. P. Plostins  
            Dr. A. Mikhail  
            Dr. J. Sahu  
            Mr. P. Weinacht  
            AMSRL-WT, Dr. A. Barrows  
            AMSRL-WT-PD, Dr. B. Burns  
            AMSRL-WT-PA,  
            Dr. T. Minor  
            Mr. M. Nusca  
            AMSRL-WT-W, Dr. C. Murphy  
            AMSRL-WT-WB, Dr. W. D'Amico  
            AMSRL-WT-NC,  
            Ms. D. Hisley  
            Mr. R. Lottero  
            AMSRL-CI-C,  
            Dr. W. Sturek  
            Dr. N. Patel  
            AMSRL-SL-C, M. Miller
- 2    Cdr, ARDEC  
      ATTN: Firing Tables, B'dg 120,  
            Mr. R. Lieske  
            Mr. R. McCoy



## USER EVALUATION SHEET/CHANGE OF ADDRESS

This Laboratory undertakes a continuing effort to improve the quality of the reports it publishes. Your comments/answers to the items/questions below will aid us in our efforts.

1. ARL Report Number ARL-TR-438 Date of Report June 1994

2. Date Report Received \_\_\_\_\_

3. Does this report satisfy a need? (Comment on purpose, related project, or other area of interest for which the report will be used.) \_\_\_\_\_  
\_\_\_\_\_  
\_\_\_\_\_

4. Specifically, how is the report being used? (Information source, design data, procedure, source of ideas, etc.) \_\_\_\_\_  
\_\_\_\_\_  
\_\_\_\_\_

5. Has the information in this report led to any quantitative savings as far as man-hours or dollars saved, operating costs avoided, or efficiencies achieved, etc? If so, please elaborate. \_\_\_\_\_  
\_\_\_\_\_  
\_\_\_\_\_

6. General Comments. What do you think should be changed to improve future reports? (Indicate changes to organization, technical content, format, etc.) \_\_\_\_\_  
\_\_\_\_\_  
\_\_\_\_\_  
\_\_\_\_\_

CURRENT  
ADDRESS

\_\_\_\_\_  
Organization

\_\_\_\_\_  
Name

\_\_\_\_\_  
Street or P.O. Box No.

\_\_\_\_\_  
City, State, Zip Code

7. If indicating a Change of Address or Address Correction, please provide the Current or Correct address above and the Old or Incorrect address below.

OLD  
ADDRESS

\_\_\_\_\_  
Organization

\_\_\_\_\_  
Name

\_\_\_\_\_  
Street or P.O. Box No.

\_\_\_\_\_  
City, State, Zip Code

(Remove this sheet, fold as indicated, tape closed, and mail.)  
(DO NOT STAPLE)

---

DEPARTMENT OF THE ARMY

OFFICIAL BUSINESS

**BUSINESS REPLY MAIL**

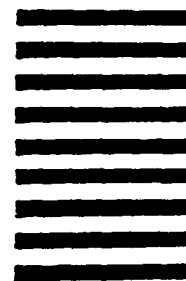
FIRST CLASS PERMIT No 0001, APG, MD

Postage will be paid by addressee.

Director  
U.S. Army Research Laboratory  
ATTN: AMSRL-OP-CI-B (Tech Lib)  
Aberdeen Proving Ground, MD 21005-5066



NO POSTAGE  
NECESSARY  
IF MAILED  
IN THE  
UNITED STATE



**SUPPLEMENTARY**

**INFORMATION**



REPLY TO  
THE ATTENTION OF

DEPARTMENT OF THE ARMY  
U.S. ARMY RESEARCH LABORATORY  
ABERDEEN PROVING GROUND, MARYLAND 21005-5066



*ERRATA*

24 August 1994

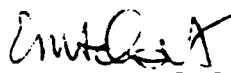
AMSRL-WT-P

MEMORANDUM FOR SEE DISTRIBUTION

SUBJECT: Correction of ARL-TR-438, Numerical Computations of Supersonic Base Flow With Special Emphasis on Turbulence Modeling, by Jubaraj Sahu, dated June 1994

1. The purpose of this memorandum is to apprise the recipients of subject report of an error in figure placement (Figures 4, 5a, 5b, and 6), pages 15 and 16. In the subject report the correct figure for Figure 4 is shown as Figure 5b; the correct figure for Figure 5b is shown as Figure 4; the correct figure for Figure 5a is shown as Figure 6; and the correct figure for Figure 6 is shown as 5a. It is requested that the incorrect pages currently in the subject report be removed and replaced with corrected pages 15 and 16 attached.
2. The U.S. Army Research Laboratory solicits input to improve the quality of reports it publishes. Comments or questions which contribute to that end should be submitted to the Director, U.S. Army Research Laboratory, ATTN: AMSRL-OP-AP-L, Aberdeen Proving Ground, MD 21005-5066.

FOR THE DIRECTOR:

*for*   
ALBERT W. HORST, JR.  
Chief  
Propulsion and Flight Division

Encl

DISTRIBUTION:

~~94-20124~~



~~94-006185~~

*ERRATA AD-A 283688*

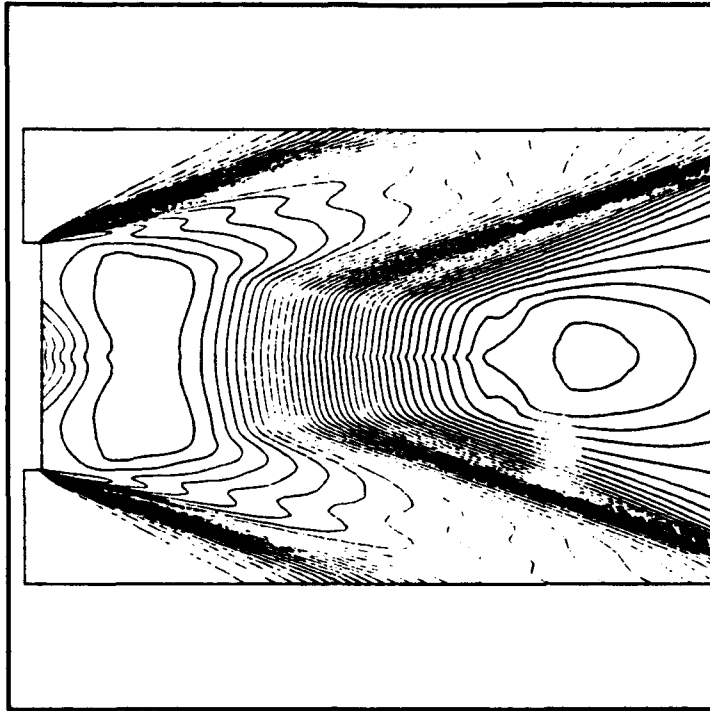


Figure 4. Computed Pressure Contours in the Base Region,  $M_{\infty} = 2.46$ ,  $\alpha=0$ , and k- $\epsilon$  Model.

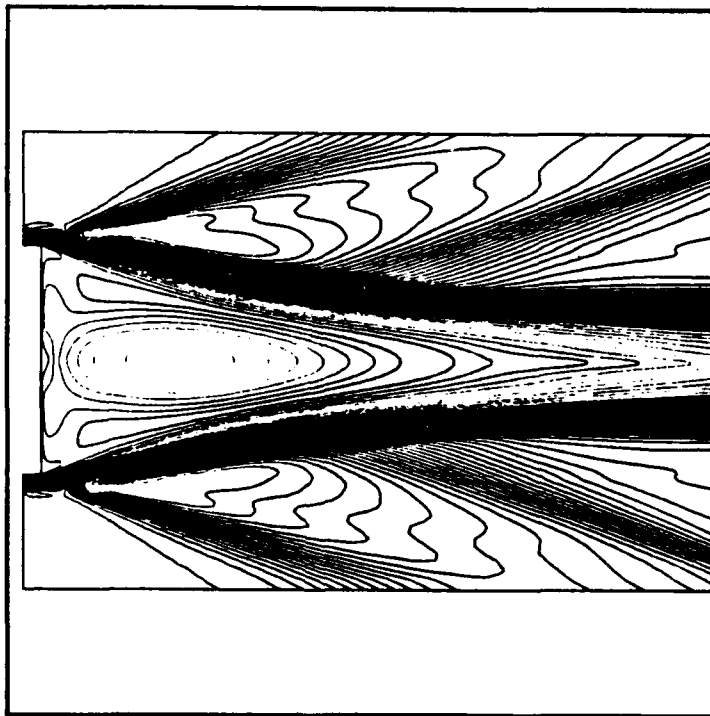


Figure 5a. Computed Mach Contours,  $M_{\infty} = 2.46$ ,  $\alpha = 0$ , and k- $\epsilon$  Model.

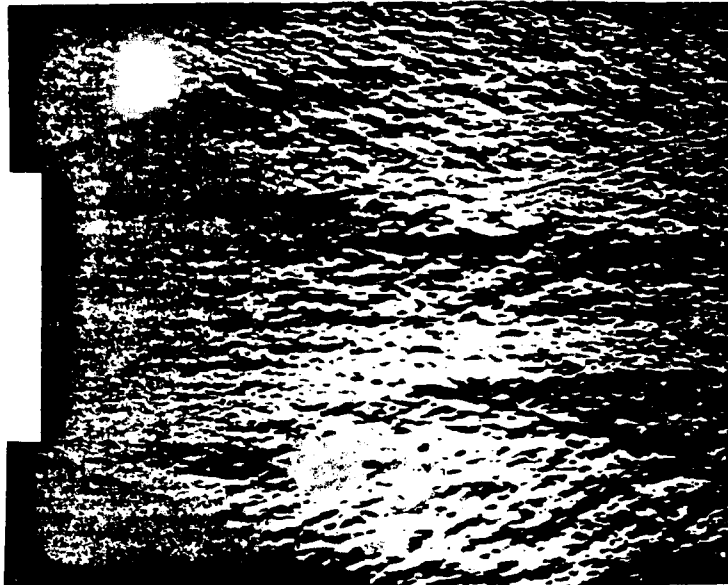


Figure 5b. Experimental Schlieren Photograph.

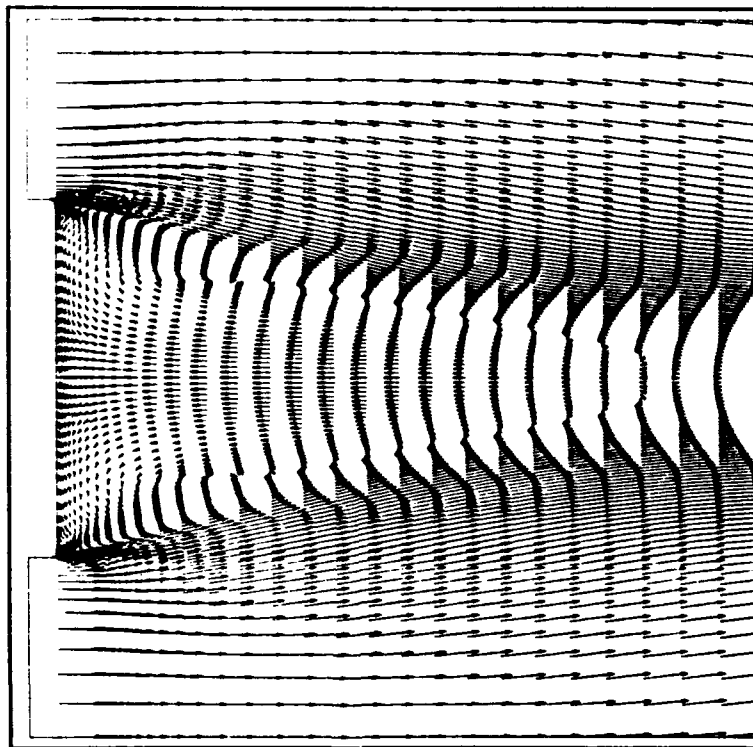


Figure 6. Velocity Vectors in the Base Region,  $M_\infty = 2.46$ ,  $\alpha = 0$ , and k- $\epsilon$  Model.